Efficient solar light photoreduction of CO_2 to hydrocarbon fuels via magnesiothermally reduced TiO_2 photocatalyst

Abdul Razzaq [a], Apurba Sinhamahapatra [a], Tong-Hyung Kang [a], Craig A. Grimes [b], Jong-Sung Yu [a,*], Su-Il In [a,*]

[a] Department of Energy Systems Engineering, DGIST, 333 Techno Jungang-daero, Hyeonpung-myeon, Dalseong-gun, Daegu, 42988, Republic of Korea
[b] Flux Photon Corporation, 116 Donmoor Court, Garner, North Carolina, 27529, United States

ABSTRACT

Elevated atmospheric CO_2 levels are recognized as a key driver of global warming. Making use of sunlight to photoreduce CO_2, in turn fabricating hydrocarbon fuels compatible with the current energy infrastructure, is a compelling strategy to minimize atmospheric CO_2 concentrations. However, practical application of such a photocatalytic system requires significant efforts for improved photoreduction performance and product selectivity. Herein, we investigate the performance of our newly developed reduced TiO_2, prepared by a reduction process using Mg in 5% H_2/Ar, for photoconversion of CO_2 and water vapor to hydrocarbons, primarily CH_4. Using Pt nanoparticles as a co-catalyst, under simulated solar light irradiation the reduced anatase TiO_2 exhibits a relatively stable performance with a threefold increase in the rate of CH_4 production (1640.58 ppm g^{-1} h^{-1}, 1.13 μmol g^{-1} h^{-1}) as compared to anatase TiO_2 nanoparticles (546.98 ppm g^{-1} h^{-1}, 0.38 μmol g^{-1} h^{-1}). The improved photocatalytic performance is attributed to enhanced light absorption, suitable band edge alignment with respect to the CO_2/CH_4 redox potential, and efficient separation of photogenerated charges. Our results suggest that the Pt-sensitized reduced TiO_2 can serve as an efficient photocatalyst for solar light CO_2 photoreduction.

© 2017 Elsevier B.V. All rights reserved.

1. Introduction

Increased atmospheric carbon dioxide (CO_2) concentrations, primarily due to the combustion of fossil fuels, is one of the preeminent obstacles faced by global society [1,2]. In this regard, numerous approaches have been investigated to control and normalize atmospheric CO_2 concentrations [3]. One of the most effective ways is to use sunlight-activated catalysis (photocatalysis) to transform CO_2 and water vapor into hydrocarbon fuels and chemicals, such as methane, ethane, methanol, carbon monoxide, and formic acid [4–6]. CO_2 photoreduction, *i.e.* "artificial photosynthesis," [4] provides a viable means for turning sunlight into a readily transportable fuel compatible with the current energy infrastructure.

To date, various photocatalytic materials have been investigated for their utility in CO_2 photoreduction, including ZnO [7], $ZnGa_2O_4$ [8], Ga_2O_3 [9], $BiVO_4$ [10], g-C_3N_4 [11], Si nanocrystals [12], GO [13] and TiO_2 [14]. Among them, TiO_2 is a widely investigated photocatalyst that possesses several comparative

advantages including excellent chemical stability, nontoxicity, corrosion resistance, abundant availability and low cost [15]. However the photocatalytic performance of TiO_2 is limited due to its relatively wider band gap (~3.2 eV for anatase), which limits light absorption to UV wavelengths comprising only 3–5% of terrestrial sunlight energy [15]. Several strategies have been investigated to enhance the solar-spectrum absorption of TiO_2, including metal and non-metal doping [16,17], coupling of low band gap materials [18,19], and dye-sensitization [20]. Co-catalyst metals such as Pt, Ag, Nb, Au, and Cu act as electron traps, or sinks, facilitating separation of photoexcited charges, in turn leading to improved photocatalytic performance [16].

Recently, Mao and co-workers reported hydrogenated TiO_2 nanocrystals [21], black in color, with a highly disordered surface layer resulting in enhanced light absorption with, in turn, improved photocatalytic activity for methylene blue degradation and hydrogen production from methanol-water. Subsequently, several studies have been done for the development of hydrogenated or reduced TiO_2 via manipulation and influence of various reaction parameters (temperature, pressure, gas composition *etc.*), synthesis methodologies, and initial TiO_2 precursors [22–25]. It is generally accepted that reduction of TiO_2 generates a large num-

ber of surface defects, Ti^{3+} ions, and oxygen vacancies, which are mainly responsible for the improved light absorption that, in turn, leading to higher photocatalytic performance [22–25]. While the utilization of the absorbed visible light resulting from these samples has proven limited, the hypothesis of those working in the field is that a controlled synthetic approach may improve the visible light activity [26,27]. To that end, we recently reported a new approach for fabrication of a defect-induced TiO_2 photocatalyst that involves magnesiothermic reduction in 5% H_2/Ar followed by acid washing [28,29]. The reduced TiO_2 exhibits better activity for visible light hydrogen production, by photocatalytic water splitting, than that previously reported for black TiO_2. In terms of CO_2 photoreduction, until now there exist but few studies employing hydrogenated/reduced TiO_2 systems, with results suggesting the oxygen vacancies and surface defects acting as electron donors can promote charge transport and CO_2 activation [30–33].

Herein we investigate the simulated solar light-driven CO_2 photoreduction with water vapor on reduced TiO_2 (RT) nanoparticles synthesized by controlled magnesiothermic reduction of commercially available anatase TiO_2 (CT) nanoparticles. Interestingly, the band edge positions of RT are found in good alignment with the CO_2/CH_4 redox potential, and hence CH_4 is produced as a dominant product with minor amounts of ethane and higher alkanes. Platinum (Pt), an electron transferring co-catalyst, is photodeposited onto the reduced TiO_2 surface for efficient separation of photogenerated charges. Optimization of Pt deposition is accomplished by preparing a series of Pt deposited RT samples in which the weight percent of Pt precursor is varied. The aforementioned requirements of broad-spectrum light absorption, efficient charge transfer, and well-aligned band edges are all achieved with the described photocatalyst system.

2. Experimental methods

2.1. Synthesis of reduced TiO_2 (RT)

The RT used in the present study was synthesized by magnesiothermic reduction in the presence of 5% H_2/Ar [28]. In a typical procedure, 1.6 g (20 mmol) of commercial nano-TiO_2 (Anatase nanoparticles purchased from Sigma-Aldrich, USA) were well-mixed with 240 mg (10 mmol) of Mg powder ($\geq$99%, Sigma-Aldrich) and heated to 650 °C (ramp 2 °C min^{-1}) for 5 h under 5% H_2/Ar in a tube furnace. After cool down, the sample was collected and washed with dilute HCl (ACS reagent, 37.0%, Sigma-Aldrich) to remove the Mg species. The Mg and Cl• free RT sample was obtained after copious washing with DI water, and then dried in a hot air oven overnight. The removal of Mg and Cl• was confirmed using X-ray photoelectron spectroscopy (XPS), see Fig. S1; the absence of Cl• was further confirmed by the AgNO$_3$ solution test. A 1:0.5 molar ratio of TiO_2 and Mg was selected, as it was previously observed this ratio produced the optimal photocatalyst for photocatalytic hydrogen production from methanol-water [28,29].

Different control samples were prepared such as: (i) CT with Mg only annealed under Ar gas named as RT(Mg); (ii) CT annealed under Ar only named as CT(Ar); and (iii) CT annealed under 5% H_2/Ar named as RT(H_2). All control samples were synthesized under conditions similar to those of the RT samples.

2.2. Synthesis of Pt sensitized reduced TiO_2 (Pt-x-RT)

Pt co-catalyst nanoparticles were deposited onto RT using photodeposition [34]. A series of Pt-x-RT samples were prepared, where x = 0.5, 0.9, 1.0, 1.2, and 2.0 represents the theoretically calculated weight percent (wt.%) of Pt with respect to a fixed amount of RT (100 mg). The desired amount of $H_2PtCl_6 \cdot 6H_2O$ (ACS

reagent, $\geq$37.50%, Sigma-Aldrich) was added to 25 ml of methanol (20 vol.%)-water solvent containing 100 mg of RT. After continuous stirring for 1 h in a closed system, the well-dispersed solution was irradiated using 300 W xenon lamp (Newport) with a 6.0 cm long IR water filter for 2 h. Finally, the Pt sensitized RT sample was thoroughly washed with deionized (DI) water and dried under vacuum at 90 °C for 12 h. Pt (1.0 wt.%) was also photodeposited on all control samples with similar procedure and tested for CO_2 photoreduction experiment.

2.3. Characterization techniques

Sample crystallinity was determined from X-ray diffraction (XRD) patterns, recorded using an X-ray diffractometer (Panalytical, Empyrean) operated at 40 kV and 30 mA with Cu Kα radiation (λ = 1.54 Å) as an X-ray source, scanned with a step degree of 0.02° and duration time of 0.5 s in the range of 2θ = 20–60°. Crystallite size of the RT and CT samples was calculated using the Scherrer equation. The light absorption of powder samples was analyzed by UV-vis diffuse reflectance spectroscopy (UV-vis DRS), using a Cary series (Cary 5000) UV-vis-near IR spectrophotometer (Agilent Technologies) with a diffuse reflection accessory in the range of 300–700 nm. Photoluminescence (PL) spectra were measured using Cary Eclipse Fluorescence Spectrophotometer (Agilent Technologies) with an excitation wavelength of λ_{ex} = 300 nm. PL measurement samples were prepared by dispersing powder samples in ethanol with a concentration of 0.5 mg ml^{-1}. Transmission electron microscopy (TEM) images were obtained using a FE-TEM (Hitachi HF-3300). Samples for TEM analysis were prepared by dispersing powder samples (0.05 mg ml^{-1}) in ethanol followed by sonication of the mixture for few minutes, with one drop of the suspension dropped onto a Ni TEM grid and allowed to dry overnight. ImageJ software was used to estimate the Pt nanoparticle size distribution and average particle size (d_{avg}) from the HR-TEM images. The surface composition, oxidation states and valence band for pure CT, RT and Pt (1.0 wt.%) sensitized RT (Pt-1.0-RT) were determined by X-ray photoelectron spectroscopy (XPS, Thermo Scientific, ESCALAB 250Xi) using Al Kα line (148606 eV) as the X-ray source. Curve fitting of the XPS spectra was performed using the Gaussian method and all XPS peaks were calibrated against the reference peak of carbon C 1s appearing at binding energy = 284.6 eV (Fig. S2). Electron paramagnetic resonance (EPR) spectra of samples CT and RT were recorded using a continuous wave X-band spectrometer (JEOL, JES-FA200), by applying a 9185.041 MHz, 0.998 mW microwave signal at −163.5 °C. A Micromeritics ASAP 2020 apparatus was used to measure the N_2 sorption isotherms at −196 °C, to investigate surface area and pore size of all samples; prior to measurement, all samples were extensively degassed at 200 °C and 20 mTorr for 300 min. The Brunauer-Emmett-Teller (BET) equation was used to calculate the surface areas for all samples in the relative pressure (P/P_0) range of 0.05–0.30. Pore size was obtained by applying the Barrett-Joyner-Halenda (BJH) equation to the desorption isotherms.

To examine possible coverage of the photocatalyst surface by intermediate species generated during the photocatalytic reactions, BET surface area and CO_2-Temperature Programmed Desorption (TPD) analysis were carried out employing representative sample Pt-1.0-RT after the 3rd cycle of a stability test, and the same sample after thermo-vacuum treatment. BET specifications were similar to those mentioned above, but to preclude high-temperature removal of sought intermediate species, a degassing temperature of 50 °C was used (20 mTorr for 300 min). CO_2-TPD profiles were measured using an AutoChem II Chemisorption analyzer (RS232 Status, Micromeritics); samples (30 mg) were treated under He gas flow (50 ml min^{-1}) at 50 °C (1 h) followed by cooling to ambient temperature, after which CO_2 gas (5% in He) was

allowed to flow (50 ml min^{-1}) through the samples for CO_2 adsorption (30 min). TPD analysis was performed under He gas flow (50 ml min^{-1}) by heating the sample to 500 °C with a rate of 20 °C min^{-1}.

2.4. Band gap and band edge estimation

Band gap (E_g) values were estimated using Tauc plots [35]. The KM function $(\alpha h\nu)^2$, where α is the absorption coefficient, h is Planck constant, and ν is frequency, was plotted against band gap energy ($E = h\nu = hc/\lambda$). Band gaps were determined by extrapolating the linear portions of the curves to y = 0. Values for the upper edge of the valence band were obtained from valence band XPS which is aligned vs. NHE. The conduction band minimum was thus obtained by subtracting the band gap value from the valence band maximum.

2.5. CO_2 photoreduction

Using a gas phase reactor, the prepared materials were investigated for their ability to promote photoconversion of CO_2 and water vapor into CH_4, see Fig. S3. Following the procedure reported earlier [36], 70 mg of photocatalyst was loaded into a stainless steel photoreactor (Volume = 15.4 cm^3) with a quartz window. CO_2 (1000 ppm in He) was allowed to pass through a water bubbler forming a mixture of CO_2 and water vapor. Prior to photoreduction experiments the reactor was repeatedly, five times, purged with CO_2 gas (1000 ppm in He) and vacuum to remove gaseous impurities. The photoreactor was illuminated with 1 sun simulated sunlight using a 100 W xenon solar simulator (Oriel, LCS-100) equipped with an AM 1.5G filter. After 1 h of continuous illumination, a sample of 500 μl was taken from photoreactor, using an argon-purged syringe, and injected into the gas chromatography (GC) unit (Shimadzu GC-2014, Restek RT-Q-Bond column, ID = 0.53 mm, length = 30 m) equipped with a flame ionization detector (FID). The time normalized rate of CH_4 formation is calculated by:

$$CH_4 \ production \ rate = \frac{amount \ of \ CH_4 \ evolved \, (ppm)}{photocatalyst \ amount \ (g) \cdot time \, (h)}$$

At least three freshly-prepared samples of each material composition were tested under similar experimental conditions. The average of the three measurements, with their standard deviation indicated by error bars, is reported as the CH_4 evolution rate. Photocatalyst stability was tested by passing the same Pt-1.0-RT sample through up to seven CO_2 photoreduction cycles. After each CO_2 photoreduction cycle the photoreactor was purged, five times, with CO_2 gas (1000 ppm in He) and vacuum, then finally refilled with $CO_2/H_2O_{(g)}$ vapor and illuminated for 1 h. To investigate the origin of the carbon intrinsic to the CH_4 evolution a control test was performed by illuminating sample Pt-1.0-RT in an $Ar/H_2O_{(g)}$ atmosphere.

2.6. $^{13}CO_2$ isotopic experiment

$^{13}CO_2$ isotopic experiments were performed to confirm CO_2 as the original source of carbon. $^{13}CO_2$ (^{13}C 99.0%), was purchased from Aldrich and diluted in pure He gas (99.999%) to give $^{13}CO_2$ with final concentration of 1000 ppm in He. The gas was then passed through a bubbler forming a mixture of $^{13}CO_2/H_2O_{(g)}$ which was introduced into the photoreactor, argon purged, loaded with Pt-1.0-RT photocatalyst (70 mg) and then illuminated.
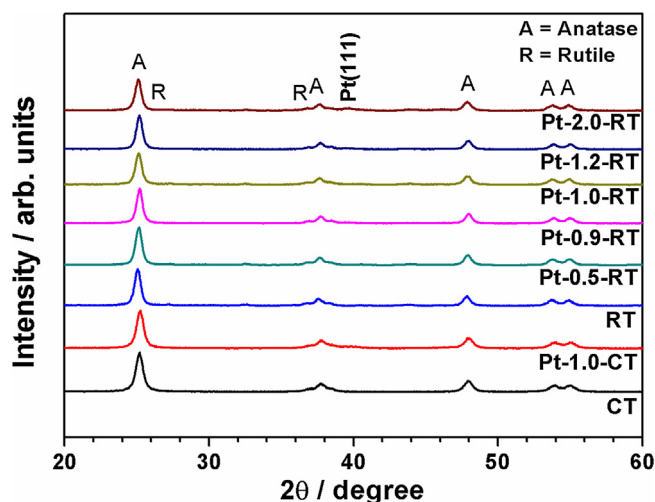

Fig. 1. (a) X-ray diffraction pattern for pure CT, RT and various Pt-x-RT samples (where x = 0.5, 0.9, 1.0, 1.2, and 2.0 corresponds to the theoretically calculated wt.% of Pt for photodeposition).

3. Results and discussion

3.1. Crystalline structure

Fig. 1 displays powder X-ray diffraction (XRD) patterns of pure CT, RT and Pt-x-RT samples. All samples exhibit a main diffraction peak of anatase (A) at a 2θ value of 25.2° corresponding to d_{101}, along with other respective minor peaks [37], suggesting no transformation or appearance of any new phase during the reduction process. A Pt peak corresponding to d_{111} is only observed in sample Pt-2.0-RT, at 2θ = 39.67° [38]. The Pt peaks are quite faint in the other Pt-x-RT samples, due possibly to the high dispersion of Pt nanoparticles or simply the low concentration. Hence further analysis was conducted to confirm the presence of Pt in these samples, as discussed later. High-resolution transmission electron microscopy (HR-TEM) images for CT and RT samples are shown in Fig. S4. HR-TEM images indicate a particle size within the range of 20–25 nm, with an interplanar spacing of 0.35 nm corresponding to the d_{101} plane of anatase TiO_2 [37]. Average crystallite size was calculated for both RT and CT samples using the Scherrer equation, see Fig. S5; a value of 12.91 nm was determined for CT, and 15.41 nm for RT, an increase in size presumably due to the heat of the magnesiothermic reduction process.

STEM elemental mapping and an HR-TEM image for a representative Pt-1.0-RT sample are presented in Fig. 2. The HR-TEM images (Fig. 2e and f) clearly demonstrate deposition of well-defined Pt nanoparticles 2–3 nm in diameter, as estimated using ImageJ software, on the RT sample surface with an interplanar d_{111} spacing of 0.22 nm [37]. The STEM-EDS elemental mapping (Fig. 2a–d) further supports the presence of homogeneously distributed Pt in the Pt-1.0-RT sample.

3.2. Surface analysis

Fig. 3a presents the high resolution XPS of region Ti 2p for both CT and RT samples, both of which exhibit the corresponding peaks for Ti 2p$_{3/2}$ and Ti 2p$_{1/2}$, with pure CT exhibiting the respective Ti 2p peaks located at 458.38 eV and 464.20 eV [39]. As compared to CT, a slight peak shifting (~0.13 eV) towards lower binding energy is observed for RT with peak broadening indicating the presence of Ti^{3+} in RT [22,30]. Further, the Ti 2p$_{3/2}$ peak of the RT samples shows a peak tail at lower binding energy, see Fig. 3b, with increased area (~6% of 2p$_{3/2}$ peak area) as compared to CT (~2% of 2p$_{3/2}$ peak
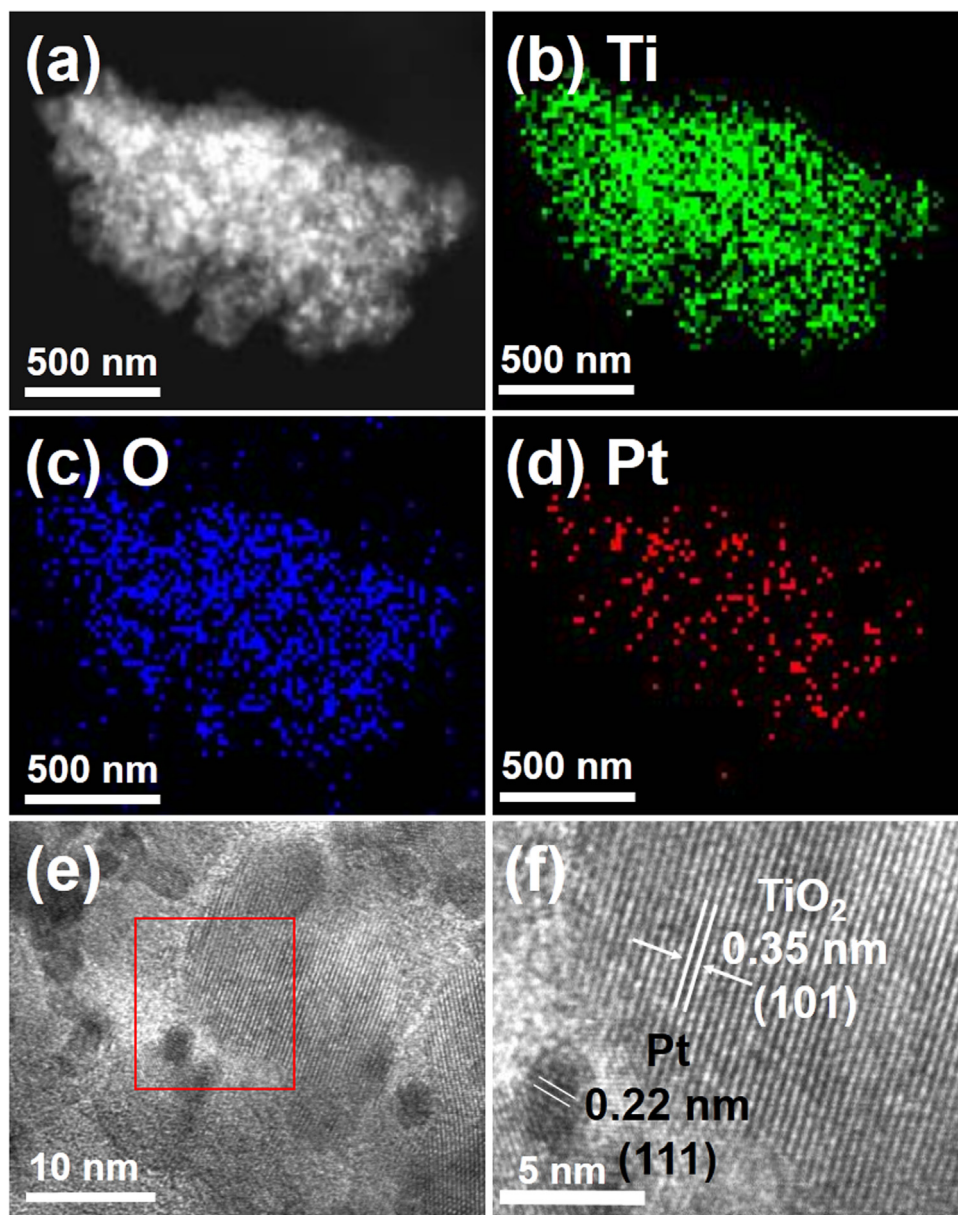
Fig. 2. (a) STEM image, and (b–d) STEM elemental mapping for a Pt-1.0-RT sample showing the presence of (b) Ti, (c) O, and (d) Pt. (e) HR-TEM image for Pt-1.0-RT sample with selected region (red square) showing (f) lattice fringes corresponding to Pt(111) and TiO$_2$(101). (For interpretation of the references to color in this figure legend, the reader is referred to the web version of this article.)

area) that can be attributed to Ti^{3+} [22,30]. The O 1s XPS spectra (Fig. 3c) of CT shows a main peak located at 529.59 eV, corresponding to Ti-O-Ti from the lattice, while the shoulder peak appearing at 530.68 eV can be assigned to non-lattice oxygen [28,40]. However, O 1s XPS spectra of RT (Fig. 3d) also shows a shift of the O 1s peaks to lower binding energies indicating the presence of Ti^{3+} [21]. As compared to sample CT, the peak appearing at the relatively higher binding energy (for non-lattice oxygen) of the RT sample possesses a larger area, as trait associated with more oxygen vacancies [28].

Sample Pt-1.0-RT (Fig. S6) exhibits similar XPS peaks for Ti 2p and O 1s as the RT sample, with the additional peak of Pt 4f (Fig. S6c), a consequence of the Pt nanoparticles. The Pt 4f spectrum can be fitted into four peaks with the main peaks appearing at 70.21 eV and 73.55 eV corresponding to the metallic Pt(0) state [41]. The Pt 4f XPS spectra for various Pt-x-RT samples (Fig. S7) demonstrates, as expected, an increase in Pt signal magnitude with increased Pt wt.%, see Table S1.

3.3. Electron paramagnetic resonance (EPR) analysis

The EPR spectra for pure CT and RT are shown in Fig. S8. The EPR spectra of sample CT shows no absorption, while the RT sample exhibits a significant and intense absorption at g = 1.975, with a shoulder peak appearing at approximately g = 1.99, traits that are assigned to the presence of Ti^{3+} ions [42,43]. In addition to these peaks, another small shoulder peak is observed at g = 2.002, which can be associated to the presence of O• species, possibly generated via interaction of O$_2$ with Ti^{3+} surface ions [44].

3.4. Optical properties

As compared to pure CT, see Fig. 4, the RT sample exhibits a slight red shift in the absorption peak, with increased absorption in the visible region (Fig. 4a). Such an extension of light absorption for the RT sample suggests a narrowing of the band gap due to formation of new energy states near the top of the valence band and bottom of
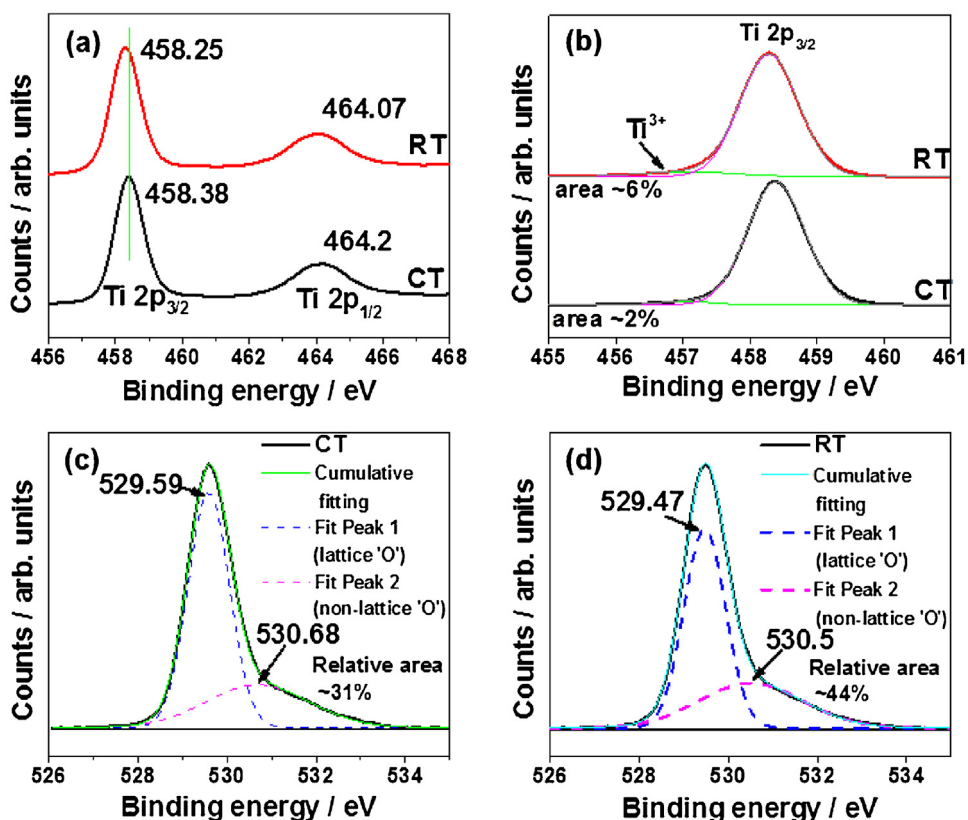
Fig. 3. X-ray photoelectron spectra (XPS) of pure CT and RT samples, regions: (a) Ti 2p, and (b) enlarged view of Ti 2p$_{3/2}$ region. Oxygen region for: (c) pure CT, and (d) RT.
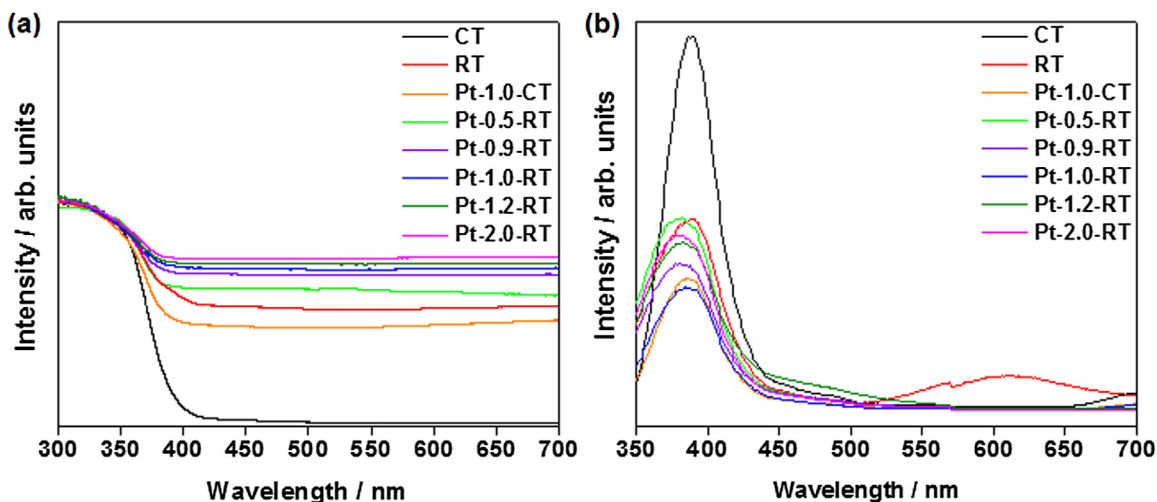

Fig. 4. (a) UV-vis DRS, and (b) Photoluminescence (PL) spectra for pure CT, Pt-1.0-CT, RT and various Pt-x-RT samples. RT shows visible range absorption due to inter-bandgap states. The PL band-to-band emission peak of sample Pt-1.0-RT is the most quenched, indicating the fastest electron extraction among all Pt-x-RT samples (where x = 0.5, 0.9, 1.0, 1.2, and 2.0 corresponds to theoretically calculated wt.% of Pt for photodeposition).

the conduction band, a behavior we hypothesize is due to oxygen vacancies or surface defects. A further increase in visible spectrum absorption was observed for Pt-x-RT, which can be attributed to localized surface plasmon resonance (LSPR) induced by the Pt nanoparticles [45]. The LSPR effect increases with Pt loading up to 1.0 wt.%, with no significant difference observed for Pt-1.2-RT and Pt-2.0-RT. It is well known that LSPR induced visible light absorption increases with Pt nanoparticle size and/or Pt amount [45–49]. We see as the Pt loading is increased from 0.5 to 1.0 wt.%, there is an increase of Pt content (Fig. S7 & Table S1) with perceptible

increase in average Pt particle size (Fig. S10), hence both parameters contributing for increased LSPR induced light absorption. For Pt 1.2 wt.% and 2.0 wt.% loaded RT samples there is no significant difference in average Pt nanoparticle size (Fig. S10), which suggests that the slight increase in visible light absorption for Pt-2.0-RT is simply associated with increased Pt content.

Fig. 4b shows photoluminescence (PL) spectra in the 350–700 nm wavelength range. Sample CT displays an intense emission peak around 390 nm, which can be attributed to the band gap transition of anatase TiO$_2$. Sample RT exhibits a significant
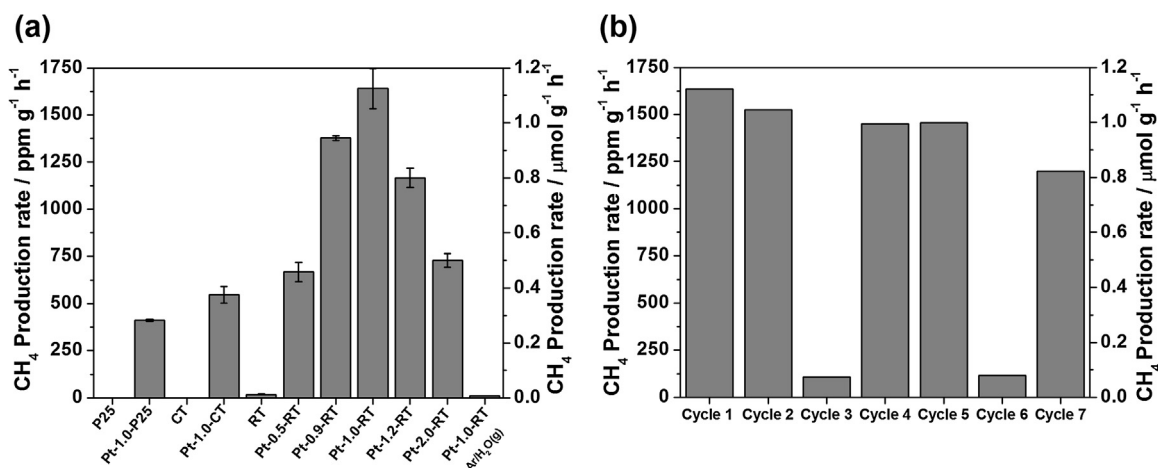
Fig. 5. (a) Methane production rate from P25 (Degussa), Pt-1.0-P25, pure CT, Pt-1.0-CT, RT, and various Pt-x-RT samples (where x = 0.5, 0.9, 1.0, 1.2, and 2.0 corresponds to theoretically calculated wt.% of Pt for photodeposition). Control test employing Pt-1.0-RT sample under $Ar/H_2O_{(g)}$ atmosphere suggests negligible CH_4. (b) Methane production rate from Pt-1.0-RT sample for seven test cycles of CO_2 photoreduction.

decrease of this peak with the appearance of another broader peak centered at 620 nm, which can be associated with RT surface defects. PL emission intensity is proportional to the photogenerated electron and hole ($e\bullet/h^+$) recombination rate. The decreased intensity of the $\lambda = 390$ nm peak for RT indicates a low $e\bullet/h^+$ recombination rate. Moreover, when Pt is loaded on the RT sample, as seen for representative sample Pt-1.0-RT, the emission intensity of the $\lambda = 390$ nm peak is further decreased. Such peak quenching indicates effective separation of the photoexcited electrons, with the Pt nanoparticles acting as electron sinks [50,51]. Among all the Pt-loaded RT samples, Pt-1.0-RT shows the lowest PL intensity implying optimal Pt content.

3.5. CO₂ photoreduction

The photocatalytic performance of the CT, RT, and Pt-x-RT samples was evaluated by testing them for photocatalytic conversion of CO_2 into hydrocarbons under AM 1.5G illumination. As discussed, photocatalytic experiments were carried out in a gas phase reactor (Fig. S3) with a mixture of $CO_{2(g)}$ and water vapor as reactants. Fig. 5a shows the photocatalytic CH_4 production rate for pure CT, RT and Pt-x-RT samples; the output species were found to be primarily methane (CH_4) with minor products of ethane (C_2H_6) and higher alkanes (C_xH_y). CT produced a negligible amount of CH_4 without Pt sensitization, whereas RT exhibited a measurable but low CH_4 yield; the CH_4 production rate is significantly improved with Pt sensitization. In particular, Pt-1.0-RT produced CH_4 at a rate of 1640.58 ppm g^{-1} h^{-1} (1.13 $\mu mol\,g^{-1}\,h^{-1}$), approximately 82 times higher than that of pure RT (18.31 ppm g^{-1} h^{-1}, 0.013 $\mu mol\,g^{-1}\,h^{-1}$) and 3 times higher than that of Pt-1.0-CT (546.98 ppm $g^{-1}\,h^{-1}$, 0.38 $\mu mol\,g^{-1}\,h^{-1}$). The photocatalytic hydrocarbon yield, and selectivity, is reported in Table S2 for all samples. Compared to Pt-1.0-CT, sample Pt-1.0-RT yielded over a factor of two increase in turnover number (TON) and over a factor of three increase in the rate of CO_2 to CH_4 conversion, see Table S3. The increase in CH_4 production rate as well as photoactivity of Pt deposited RT can be understood considering: (i) improved RT visible light absorption due to a reduction in band gap and reduced recombination of photogenerated charge; and (ii) enhanced charge separation due to the Pt nanoparticles. When the Pt loading is increased from 0.5 to 1.0 wt.% the CH_4 production also increases, however the rate decreases for 1.2 and 2.0 wt.% Pt loaded samples. A control experiment employing Pt-1.0-RT under similar conditions in the presence of $Ar/H_2O_{(g)}$ produced negligible amounts of hydro-

carbons, suggesting no involvement of any organic impurities on the surface of the samples.

To help understand our results surface area and pore size distributions of all Pt-x-RT samples were investigated, see Fig. S9 and Table S4; all samples possess essentially identical surface area and pore structure. However, the HR-TEM images (Fig. S10) reveal a gradual increase in size and agglomeration of the Pt nanoparticles with loading amount. We submit that as the Pt loading was increased from 0.5 to 1.0 wt.% the amount of Pt nanoparticles was increased with good dispersion, while on further increasing the Pt loading above 1.0 wt.% the size and agglomeration of the Pt nanoparticles increased, in turn increasing the diffusion length of the separated electrons and hence increasing recombination [46]. This supposition is supported by the PL spectra (Fig. 4b), where Pt-1.2-RT and Pt-2.0-RT show higher emission peaks than the Pt-1.0-RT sample.

The stability of sample Pt-1.0-RT was investigated by repeated testing of the same sample (Fig. 5b). While similar amounts of CH_4 were obtained for the 1st and 2nd cycles, activity decreased sharply for the 3rd cycle. The sample was then reactivated by heating at 90 °C under vacuum for 3 h, with photocatalytic activity almost fully recovered for the 4th and 5th cycles. During the 6th cycle the activity decreased in a pattern similar to that of the 3rd cycle, hence the sample was again subjected to vacuum heat treatment, whereupon for the 7th cycle photocatalytic activity was found to be approximately 76% that of the 1st cycle. The mechanism for photocatalyst deactivation is not exactly known, however literature suggests coverage of active sites by intermediate products [52–54].

Fig. S11 shows the BET surface area of a Pt-1.0-RT sample after the 3rd stability test cycle, and after subsequent thermo-vacuum treatment; both N_2 sorption curves demonstrate type IV isotherms with H3 hysteresis loops [55]. The BET surface area for the used sample (36.80 $m^2\,g^{-1}$) is significantly less than that after thermo-vacuum treatment (44.94 $m^2\,g^{-1}$). Such a decrease in surface area can be ascribed to coverage of the sample surface by intermediate species, in turn influencing the photocatalytic performance. Fig. S12 shows the CO_2-TPD profiles for both samples; the thermo-vacuum treated sample shows greater CO_2 adsorption with increased intensity peaks in the region of weak basic sites (~100–250 °C) [56–58] that can be attributed to desorbed CO_2 [58,59], indicating favorable interaction of the gas with the photocatalyst surface. In contrast the used sample (after 3rd cycle) exhibits a decreased peak intensity in the weak basic sites region, indicating poor CO_2 adsorption, with a broad hump in the medium basic sites region (~250–400 °C) [56,58]
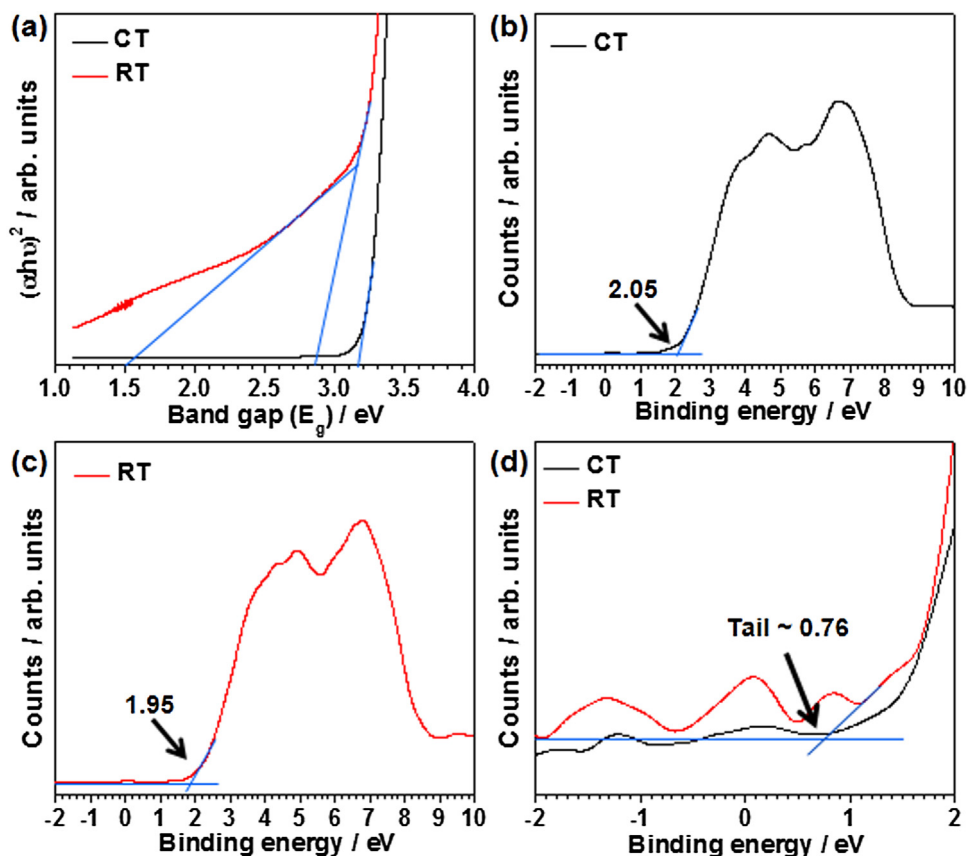
Fig. 6. (a) Band gap estimation using Tauc plot and (b-d) valence band XPS for pure CT and RT. The RT shows a VB band tail up to 0.76 eV hence further shifting VB upward.
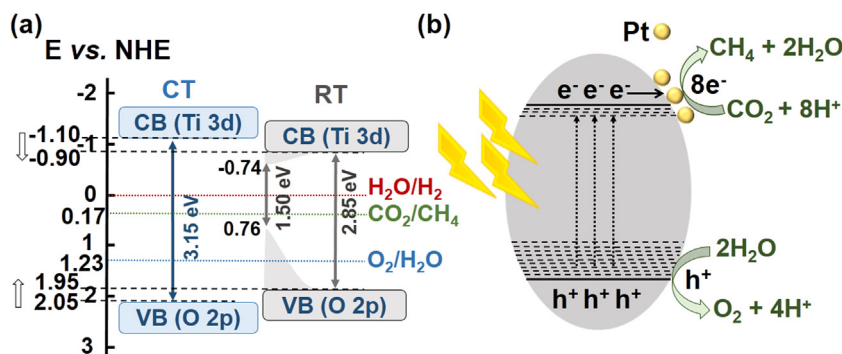

Fig. 7. (a) Energy level diagram (potential *vs.* NHE) and (b) proposed mechanism for CO_2 photoreduction.

associated with bidentate carbonate species, possibly formed by intermediate species on the photocatalyst surface [54]. The CH_4 production rate yielded by various control samples is shown in Fig. S13. The RT samples show a superior CH_4 yield, with the Pt sensitized RT samples exhibiting photocatalytic performance competitive with previously reported reduced TiO_2 samples (Table S5).

Fig. S14, shows the gas chromatogram of the $^{13}CO_2$ isotopic experiment employing sample Pt-1.0-RT; peaks at $m/z = 45$ and $m/z = 17$ are observed, which are associated, respectively, with $^{13}CO_2$ and $^{13}CH_4$. GC–MS analysis shows the formation of $^{13}CH_4$ from $^{13}CO_2$, confirming the CH_4 produced during the photochemical reaction predominately originates from CO_2.
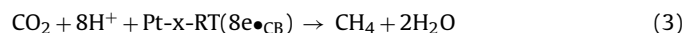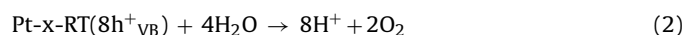
3.6. Mechanism for CO_2 photoreduction

To help understand the process by which CO_2 is photocatalytically converted into CH_4 the CT and RT band gaps, obtained using

Tauc plots [35], and VB positions were analyzed, see Fig. 6. It can be clearly seen that CT exhibits a band gap of 3.15 eV, while RT shows a band gap of 2.85 eV. However, the RT Tauc plot displays an additional slope that leads to a lower band value gap of 1.50 eV, suggesting the formation of CB and VB tails due to a new density of states introduced during reduction [44]. VB XPS data indicates the top of the VB for CT is 2.05 eV (Fig. 6b), and 1.95 eV for RT (Fig. 6c) with a tail up to 0.76 eV (Fig. 6d). The band gap is narrowed via the reduction process through introduction of Ti^{3+} and O vacancies/surface defects [21,44].

A schematic illustration of the probable energy level diagram (potential *vs.* NHE) and CO_2 photoreduction scheme can be seen in Fig. 7a, displaying the relative positions of CB and VB for CT and RT, and redox potentials for CO_2/CH_4 and O_2/H_2O. RT appears a more efficient photocatalyst for CO_2 photoreduction, possessing a CB minimum at -0.90 eV with a CB tail up to -0.74 eV, and a corresponding VB maximum at 1.95 eV with a VB tail up to 0.76 eV.

The downward shifted CB bottom lies above the redox potential of CO_2/CH_4 (0.17 eV), whereas the VB top lies slightly above the O_2/H_2O redox potential (1.23 eV) [60].

As suggested by Fig. 7b, under illumination the photogenerated $e\bullet/h^+$ pairs are generated via band to band and sub-band gap excitations; the photoexcited electrons are injected to the CB and efficiently extracted by the Pt nanoparticles. Taking into mind proton assisted multi-electron processes for CO_2 photoreduction [6,60], these photoexcited electrons can react with surface adsorbed CO_2 in the presence of protons (H^+, produced in water oxidation) to evolve CH_4 as a primary product. Concurrently, the VB generated holes are involved in water oxidation, producing O_2 and protons (H^+). The suggested reactions involved in CO_2 photoreduction to CH_4 can be summarized as follows:

$$Pt\text{-}x\text{-}RT + h\nu(\text{sunlight}) \rightarrow Pt\text{-}x\text{-}RT(e\bullet_{CB}) + Pt\text{-}x\text{-}RT(h^+_{VB}) \tag{1}$$

$$Pt\text{-}x\text{-}RT(8h^+_{VB}) + 4H_2O \rightarrow 8H^+ + 2O_2 \tag{2}$$

$$CO_2 + 8H^+ + Pt\text{-}x\text{-}RT(8e\bullet_{CB}) \rightarrow CH_4 + 2H_2O \tag{3}$$

4. Conclusions

Reduced TiO_2 is prepared by a two-step method, magnesiothermic reduction in 5% H_2/Ar followed by acid washing, and investigated with respect to its utility in CO_2 photoreduction to CH_4 under simulated solar light (1 sun, AM 1.5G). The improved light absorption and suitable band edge position of reduced TiO_2, sensitized with photodeposited Pt nanoparticles, results in a significant enhancement of CH_4 evolution. The reduced TiO_2 sample with 1.0 wt.% of Pt yielded a maximum photocatalytic CH_4 yield of 1640.58 ppm g^{-1} h^{-1} (1.13 μmol g^{-1} h^{-1}), three times higher than anatase TiO_2 (CT) and four times higher than commercial P25, both with a similar loading of Pt co-catalyst. We believe our material design approach offers significant opportunities for developing enhanced, high-performance photocatalytic materials.

Acknowledgements

Appendix A. Supplementary data

Supplementary data associated with this article can be found, in the online version, at http://dx.doi.org/10.1016/j.apcatb.2017.05.028.

References

[1] S.E. Schwartz, Energy Environ. Sci. 1 (2008) 430–453.
[2] T.F. Stocker, A. Schmittner, Nature 388 (1997) 862–865.
[3] E.V. Kondratenko, G. Mul, J. Baltrusaitis, G.O. Larrazabal, J. Perez-Ramirez, G.O. Larrazábal, J. Pérez-Ramírez, Energy Environ. Sci. 6 (2013) 3112–3135.
[4] A.D. Handoko, K. Li, J. Tang, Curr. Opin. Chem. Eng. 2 (2013) 200–206.
[5] A. Dhakshinamoorthy, S. Navalon, A. Corma, H. Garcia, Energy Environ. Sci. 5 (2012) 9217–9233.
[6] S. Xie, Q. Zhang, G. Liu, Y. Wang, Chem. Commun. 52 (2015) 35–59.
[7] G. Mahmodi, S. Sharifnia, F. Rahimpour, S.N. Hosseini, Sol. Energy Mater. Sol. Cells 111 (2013) 31–40.
[8] S.C. Yan, S.X. Ouyang, J. Gao, M. Yang, J.Y. Feng, X.X. Fan, L.J. Wan, Z.S. Li, J.H. Ye, Y. Zhou, Z.G. Zou, Angew. Chem. Int. Ed. 49 (2010) 6400–6404.
[9] H. Tsuneoka, K. Teramura, T. Shishido, T. Tanaka, J. Phys. Chem. C 114 (2010) 8892–8898.
[10] J. Mao, T. Peng, X. Zhang, K. Li, L. Zan, Catal. Commun. 28 (2012) 38–41.
[11] J. Mao, T. Peng, X. Zhang, K. Li, L. Ye, L. Zan, Catal. Sci. Technol. 3 (2013) 1253–1260.
[12] F. Peng, J. Wang, G. Ge, T. He, L. Cao, Y. He, H. Ma, S. Sun, Mater. Lett. 92 (2013) 65–67.
[13] H.C. Hsu, I. Shown, H.Y. Wei, Y.C. Chang, H.-Y. Du, Y.-G. Lin, C.-A. Tseng, C.-H. Wang, L.C. Chen, Y.-C. Lin, K.H. Chen, Nanoscale 5 (2013) 262–268.
[14] L. Liu, H. Zhao, J.M. Andino, Y. Li, ACS Catal. 2 (2012) 1817–1828.
[15] M.D. Hernández-Alonso, F. Fresno, S. Suárez, J.M. Coronado, Energy Environ. Sci. 2 (2009) 1231–1257.
[16] O.K. Varghese, M. Paulose, T.J. LaTempa, C.A. Grimes, Nano Lett. 9 (2009) 731–737.
[17] S.K. Parayil, A. Razzaq, S.M. Park, H.R. Kim, C.A. Grimes, S.-I. In, Appl. Catal. A: Gen. 498 (2015) 205–213.
[18] K. Kim, A. Razzaq, S. Sorcar, Y. Park, C.A. Grimes, S.-I. In, RSC Adv. 6 (2016) 38964–38971.
[19] S.-I In, D.D. Vaughn, R.E. Schaak, Angew. Chem. Int. Ed. 51 (2012) 3915–3918.
[20] D. Chatterjee, A. Mahata, Appl. Catal. B: Environ. 33 (2001) 119–125.
[21] X. Chen, L. Liu, P.Y. Yu, S.S. Mao, Science 331 (2011) 746–750.
[22] S. Hoang, S.P. Berglund, N.T. Hahn, A.J. Bard, C.B. Mullins, J. Am. Chem. Soc. 134 (2012) 3659–3662.
[23] H. Lu, B. Zhao, R. Pan, J. Yao, J. Qiu, L. Luo, Y. Liu, RSC Adv. 4 (2014) 1128–1132.
[24] X. Yu, B. Kim, Y.K. Kim, ACS Catal. 3 (2013) 2479–2486.
[25] A. Danon, K. Bhattacharyya, B. Vijayan, J. Lu, D. Sauter, K. Gray, P. Stair, E. Weitz, ACS Catal. 2 (2012) 45–49.
[26] Y.H. Hu, Angew. Chem. Int. Ed. 51 (2012) 12410–12412.
[27] X. Chen, L. Liu, F. Huang, Chem. Soc. Rev. 44 (2015) 1861–1885.
[28] A. Sinhamahapatra, J.-P. Jeon, J.-S. Yu, Energy Environ. Sci. 8 (2015) 3539–3544.
[29] A. Sinhamahapatra, J.-P. Jeon, J. Kang, B. Han, J.-S. Yu, Sci. Rep. 6 (2016) 27218.
[30] Y. Yan, M. Han, A. Konkin, T. Koppe, D. Wang, T. Andreu, G. Chen, U. Vetter, J.R. Morante, P. Schaaf, J. Mater. Chem. A 2 (2014) 12708–12716.
[31] K. Sasan, F. Zuo, Y. Wang, P. Feng, Nanoscale 7 (2015) 13369–13372.
[32] L. Liu, Y. Jiang, H. Zhao, J. Chen, J. Cheng, K. Yang, Y. Li, ACS Catal. 6 (2016) 1097–1108.
[33] B. Han, W. Wei, L. Chang, P. Cheng, Y.H. Hu, ACS Catal. 6 (2016) 494–497.
[34] Z. Jiang, Z. Zhang, W. Shangguan, M.A. Isaacs, L.J. Durndell, C.M.A. Parlett, A.F. Lee, Catal. Sci. Technol. 6 (2016) 81–88.
[35] J. Tauc, R. Grigorovici, A. Vancu, Phys. Status Solidi 15 (1966) 627–637.
[36] H.R. Kim, A. Razzaq, H.J. Heo, S.-I In, Rapid Commun. Photosci. 2 (2013) 64–66.
[37] P.A. Sedach, T.J. Gordon, S.Y. Sayed, T. Fürstenhaupt, R. Sui, T. Baumgartner, C.P. Berlinguette, J. Mater. Chem. 20 (2010) 5063–5069.
[38] D. Wang, H.L. Xin, R. Hovden, H. Wang, Y. Yu, D.A. Muller, F.J. DiSalvo, H.D. Abruña, Nat. Mater. 12 (2012) 81–87.
[39] Z. Wang, C. Yang, T. Lin, H. Yin, P. Chen, D. Wan, F. Xu, F. Huang, J. Lin, X. Xie, M. Jiang, Energy Environ. Sci. 6 (2013) 3007–3014.
[40] M.C. Biesinger, B.P. Payne, A.P. Grosvenor, L.W.M. Lau, A.R. Gerson, R.S.C. Smart, Appl. Surf. Sci. 257 (2010) 887–898.
[41] C. Dablemont, P. Lang, C. Mangeney, J.Y. Piquemal, V. Petkov, F. Herbst, G. Viau, Langmuir 24 (2008) 5832–5841.
[42] C.P. Kumar, N.O. Gopal, T.C. Wang, M.-S. Wong, S.C. Ke, J. Phys. Chem. B 110 (2006) 5223–5229.
[43] F. Zuo, L. Wang, T. Wu, Z. Zhang, D. Borchardt, P. Feng, J. Am. Chem. Soc. 132 (2010) 11856–11857.
[44] A. Naldoni, M. Allieta, S. Santangelo, M. Marelli, F. Fabbri, S. Cappelli, C.L. Bianchi, R. Psaro, V. Dal Santo, J. Am. Chem. Soc. 134 (2012) 7600–7603.
[45] D. Manchon, J. Lermé, T. Zhang, A. Mosset, C. Jamois, C. Bonnet, J.-M. Rye, A. Belarouci, M. Broyer, M. Pellarin, E. Cottancin, Nanoscale 7 (2015) 1181–1192.
[46] W.N. Wang, W.J. An, B. Ramalingam, S. Mukherjee, D.M. Niedzwiedzki, S. Gangopadhyay, P. Biswas, J. Am. Chem. Soc. 134 (2012) 11276–11281.
[47] N. Zhang, C. Han, Y.-J. Xu, J.J. Foley IV, D. Zhang, J. Codrington, S.K. Gray, Y. Sun, Nat. Photon. 8 (2016) 473–482.
[48] S.-F. Hung, Y.-C. Yu, N.-T. Suen, G.-Q. Tzeng, C.-W. Tung, Y.-Y. Hsu, C.-S. Hsu, C.-K. Chang, T.-S. Chan, H.-S. Sheu, J.-F. Lee, H.-M. Chen, Chem. Commun. 52 (2016) 1567–1570.
[49] J. Yu, L. Qi, M. Jaroniec, J. Phys. Chem. C 114 (2010) 13118–13125.
[50] J.S. Jang, S.H. Choi, H.G. Kim, J.S. Lee, J. Phys. Chem. C 112 (2008) 17200–17205.
[51] Q. Gu, J. Long, H. Zhuang, C. Zhang, Y. Zhou, X. Wang, Phys. Chem. Chem. Phys. 16 (2014) 12521–12534.
[52] M. Li, L. Zhang, M. Wu, Y. Du, X. Fan, M. Wang, L. Zhang, Q. Kong, J. Shi, Nano Energy 19 (2016) 145–155.
[53] F. Saladin, I. Alxneit, J. Chem. Soc. Faraday Trans. 93 (1997) 4159–4163.
[54] Y. Ji, Y. Luo, ACS Catal. 6 (2016) 2018–2025.
[55] R.C.R. Santos, D.M.V. Braga, A.N. Pinheiro, E.R. Leite, V.N. Freire, E. Longhinotti, A. Valentini, Catal. Sci. Technol. 6 (2016) 4986–5002.
[56] X. Tang, F. Gao, Y. Xiang, H. Yi, S. Zhao, X. Liu, Y. Li, Ind. Eng. Chem. Res. 54 (2015) 9116–9123.
[57] Y.Y. Li, M.M. Wan, X.D. Sun, J. Zhou, Y. Wang, J.H. Zhu, J. Mater. Chem. A 3 (2015) 18535–18545.
[58] M. Kruk, M. Jaroniec, Chem. Mater. 13 (2001) 3169–3183.
[59] K.-P. Yu, W.-Y. Yu, M.-C. Kuo, Y.-C. Liou, S.-H. Chien, Appl. Catal. B: Environ. 84 (2008) 112–118.
[60] X. Chang, T. Wang, J. Gong, Energy Environ. Sci. 9 (2016) 2177–2196.